

Article

Dental Imaging Using Mesoscopic Fluorescence Molecular Tomography: An *ex Vivo* Feasibility Study

Feixiao Long ¹, Mehmet S. Ozturk ¹, Mark S. Wolff ², Xavier Intes ¹ and Shiva P. Kotha ^{1,*}

¹ Department of Biomedical Engineering, Rensselaer Polytechnic Institute, 110 8th Street, Troy, NY 12180, USA; E-Mails: longf@rpi.edu (F.L.); ozturm@rpi.edu (M.S.O.); intesx@rpi.edu (X.T.)

² Department of Cariology and Comprehensive Care, New York University College of Dentistry, 345 East 24th Street, 10th Floor, New York, NY, 10010, USA; E-Mail: mark.wolff@nyu.edu

* Author to whom correspondence should be addressed; E-Mail: kothas2@rpi.edu; Tel.: +518-276-4388.

Received: 30 October 2014; in revised form: 27 November 2014 / Accepted: 27 November 2014 / Published: 3 December 2014

Abstract: Some dental lesions are difficult to detect with traditional anatomical imaging methods, such as, with visual observation, dental radiography and X-ray computed tomography (CT). Therefore, we investigated the viability of using an optical imaging technique, Mesoscopic Fluorescence Molecular Tomography (MFMT) to retrieve molecular contrast in dental samples. To establish feasibility of obtaining 3-D images in teeth using MFMT, molecular contrast was simulated using a dye-filled capillary that was placed in the lower half of human tooth *ex vivo*. The dye and excitation wavelength were chosen to be excited at 650–660 nm in order to simulate a carious lesion. The location of the capillary was varied by changing the depth from the surface at which the dye, at various concentrations, was introduced. MFMT reconstructions were benchmarked against micro-CT. Overall; MFMT exhibited a location accuracy of ~15% and a volume accuracy of ~15%, up to 2 mm depth with moderate dye concentrations. These results demonstrate the potential of MFMT to retrieve molecular contrast in 3-D in highly scattering tissues, such as teeth.

Keywords: dental imaging; mesoscopic molecular fluorescence tomography; laminar optical tomography; Monte Carlo

1. Introduction

Dental caries (tooth decay) is the most prevalent dental disease encountered in clinical dentistry [1] with a prevalence of 92% of adults between 20 and 64 years having developed caries in permanent teeth [2]. Diagnosis of caries is usually performed utilizing visual and/or tactile examinations and is supplemented by the use of dental radiographs. Diagnosis based only on tactile and visual inspections exhibit poor sensitivity, with 25% to 42% of the lesions going undetected, particularly in the approximal region [3–5]. Dental radiographs (X-rays) have shown potential in identifying early dental caries before the caries is otherwise visible, particularly in cases where caries occurs between teeth. However, the detection of carious lesions utilizing conventional 2-D X-radiography remains challenging [6]. This is because conventional 2-D radiographs provide limited information and sensitivity, with the appearance of a lesion being impacted by projection geometry and size [7,8]. Cone beam computed tomography (CBCT), which has been used for implant placement, orthodontics, and surgery, may provide improved detection and sensitivity of these lesions at the expense of greater radiation exposure to sensitive tissues around the head and neck [9]. Even clinically approved products which offer exceptional panoramic views of the jaw such as cone-beam tomography scanners (e.g., ILUMA™ Ultra Cone Beam Scanner, GE USA and 3D Accuitomo, J. Morita USA), have limited use due to concerns of excess radiation dosage [9–11]. Alternative imaging modalities that reveal tissue structure have also been investigated. For instance, Crawley *et al.* proposed dental tomography with THz radiation, which is known to be non-ionizing and harmless. This modality was promising in imaging enamel thickness but it could not be applied to dental caries detection due to its depth limitation (<1 mm) and high equipment cost [12,13].

All of the techniques mentioned above rely on structural imaging for identification of dental abnormalities. However, early stage of carious lesions is associated with demineralization of enamel before leading to a cavitation. Therefore, other kinds of contrast mechanisms may be leveraged to detect and locate dental caries. Optical imaging techniques have been developed to detect carious lesions by exploiting the way white light passes through the teeth (trans-illumination) and how specific wavelength light reacts with the molecular changes in the dental tissue (laser fluorescence). These diagnostic techniques are usually based on optical contrast variations elicited by significant bacterial colonization and/or byproducts of bacteria activity. The commercial system, Diagnodent™, is based on changes in fluorescence of light irradiated on tooth surfaces resulting from porphyrins that are produced by bacteria that populate carious lesions, in which the bacteria fluorescence bands are in the region 580–600 nm, with another peak around 635 nm [14]. This system detects occlusal dentinal lesions with greater success than conventional methods [15], but is not able to discern the depth and severity of early lesions [16]. Another quantitative light-induced fluorescence (QLF) system is based on detecting the decrease in auto-fluorescence generated by aromatic amino acids as a result of bacterial activity in lesions, when irradiated with different wavelengths of light [17]. When QLF has been used to detect and longitudinally monitor enamel lesions, the sensitivity and specificity of the technique is 64% and 55% for smooth surface and occlusal lesions, respectively [18]. However, QLF systems, which aim at detecting a decrease in the autofluorescence signal, are confounded with signals associated with a loss of mineral volume [19]. Moreover, as QLF is unable to retrieve the depth and structure of the lesion, QLF does not meaningfully improve above the diagnostic abilities of

conventional methods [20]. Finally, trans-illumination, in which attenuation of visible light transmitted through the tooth is detected, has been used to detect interproximal, smooth and occlusal lesions [21,22]. Attenuation of light through the tooth structure, resulting primarily from light scattering, is confounded by multiple variables in tooth structures. In addition, trans-illumination does not provide 3-D information, and are unable to detect lesion depth [23].

The main common limitation that the above mentioned optical imaging techniques share is their lack of capability to resolve depth which leads to confounding results. Herein, we investigate the potential for dental imaging of a novel 3-D optical modality that has sensitivity to functional and molecular contrast and operates in the mesoscopic regime with high resolution, namely Laminar Optical Tomography (LOT) or Mesoscopic Fluorescence Molecular Tomography (MFMT). It is noted that optical systems based on confocal [24,25] and multi-photon microscopy [26], optical coherence tomography [27,28] are also being evaluated for use in 3-D diagnosis of lesions, but, these lack the depth of penetration or require expensive components for imaging. LOT/MFMT is a new implementation of diffuse optical tomography that offers high resolution (<0.2 mm) in thick (~ 2.5 mm) tissue [29]. Recently, LOT/MFMT has been developed into a non-contact, high resolution fast optical imaging modality [30] that can image functional [31,32] and fluorescence probes *in vitro* [33–35] and *in vivo* [36,37]. LOT/MFMT technology has not been applied to tissue exhibiting a high scattering coefficient such as teeth [38]. This *ex vivo* study is intended to define detection parameters and limitations of MFMT to help demonstrate the potential of MFMT to accurately retrieve the distribution of a fluorescence marker in human teeth. As an initial step towards applying MFMT to detect *in vivo* dental lesions in 3-D, the performance of MFMT is validated by co-registration of the reconstructed volume with micro-CT.

2. Materials and Methods

2.1. Sample Preparation

The initial determination of MFMT for dental imaging, required the development of an *ex vivo* caries model to establish feasibility and performance [10,16,39–43]. Extracted molar teeth were obtained from local dental clinics with appropriate institutional biosafety committee (IBC) and institutional review board (IRB) approvals. A relatively flat surface of the tooth was selected to be imaged with the MFMT system (Figure 1a). To mimic the uptake of a molecular probe within the pulp region of the teeth, the specimens were drilled to insert 1.5 mm diameter capillaries filled with a fluorescence probe (Figure 1b). Alexa Fluor 660 (Succinimidyl Ester, Life Tech Inc., USA) was used as the fluorophore. Alexa Fluor 660 has peak absorption at 660 nm and peak emission at 690 nm, and hence, is suited for use as a contrast agent to simulate a lesion. It is noted that commercially available systems, such as the DiagnodentTM, uses an excitation wavelength of 655 nm and measures fluorescence, because carious tissue induces a greater fluorescence at these wavelengths in comparison to intact tissues [44]. To investigate the ability of MFMT to detect and identify lesions (bacterial loads at different depths and loss of hydroxyapatite), holes were drilled at depths of 1 mm, 2 mm, and 3 mm from the surface that is exposed to incident light. Various concentrations of dye, 26 μM , 13 μM and 6.5 μM were placed in the holes to simulate different bacterial fluorescence. The concentration of dye

was varied to determine the minimum contrast that could be detected using the technique. Note that holes were drilled at locations where enamel is absent and functional changes are expected.

Specimens were marked to assure that MFMT and micro-CT were both sampling the same region. The regions of the tooth to be evaluated were identified by fiducial markers (hollow hemispheres filled with Play-Doh (Hasbro, USA) positioned on the surface of the teeth to demarcate the four corners of the optical field of view (FOV) on the imaged surface. The Play-Doh, in the holes, acted as an optical contrast agent to identify their location in the optical raw data, which enabled accurate registration of the MFMT with micro-CT. To prevent motion of tooth during transport between the non-concurrent optical and X-ray CT imaging sessions, teeth were embedded in solidified (4%) agar solution (Agarose, Sigma-Aldrich, USA) (Figure 1a).

Figure 1. Phantom used in the experiment: (a) red shaded area on the tooth surface indicates the field-of-view (FOV, 6 mm by 4 mm). (b) Side view of phantom to show the hole used to hold capillary. (c) Markers at the corner of FOV.

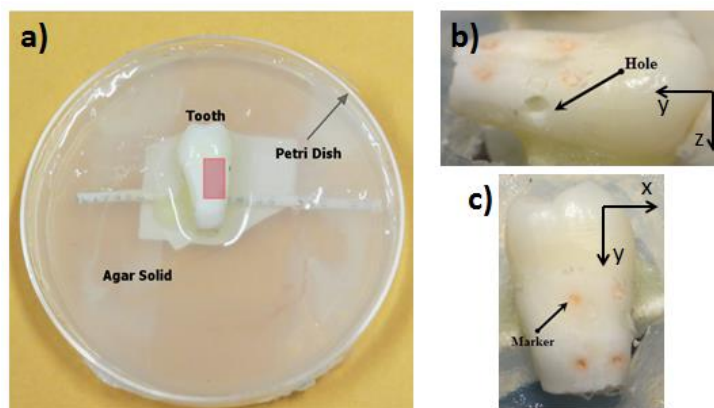
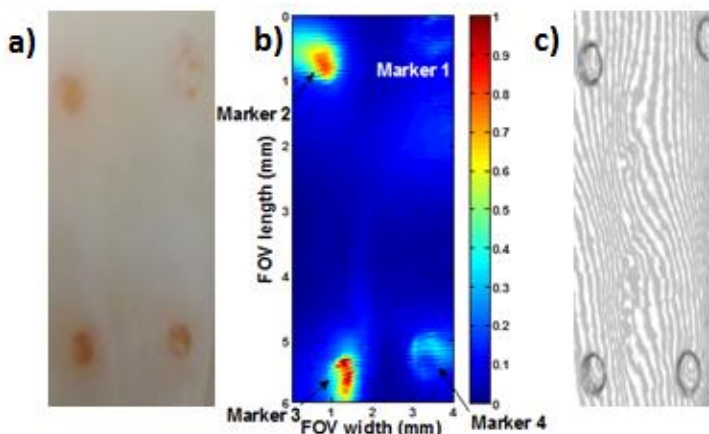


Figure 2. Image comparisons (FOV) between different modalities and white light photo of real tooth: (a) Photo of real teeth. (b) MFMT background image without the fluorescence signal. (c) Reconstructed surface of teeth using micro-CT (Some distortions may happen due to directly capture from 3-D image).

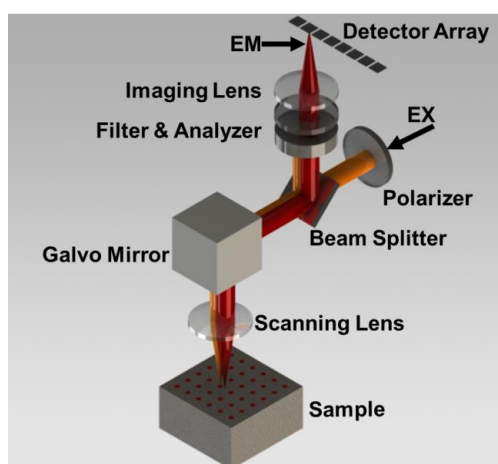


The micro-CT (Medical Viva CT40; Scanco; Switzerland) is equipped with a micro-focus X-ray cone beam source with 50–70 kVp and 8 W (160 μ A) power. 70 kVp voltage setting was used in the scanning. The standard setting was employed with 38 μ m resolution; resulting in an acquisition time of roughly 30 min. This will generate 300–400 slices of images based on the length of different teeth. The slices were then read by Matlab or ImageJ. Because the markers are clearly seen (Figure 2c), no further image processing is needed.

2.2. Optical Imaging System

Mesoscopic Fluorescence Molecular Tomography (MFMT) is an epi-fluorescence, noncontact imaging technique that is based on raster scanning of a light beam over the sample. The optical set-up is similar to a typical confocal microscopy based system, but, with offset detectors to collect diffused light [29]. These discrete detectors, which are placed radial to the irradiation point (*i.e.*, point at which light is injected into the sample), collect the emitted light. Light collected from these detectors enables probing of light propagation (scattering and absorption) from different depths, with detectors placed farther away detecting light that has penetrated deeper. This principle originates from the photon propagation model in turbid media (turbid media has scattering coefficient much larger than absorption coefficient). This model suggests that the distance between source and detector is proportional with the depth from which an individual detector collects signal [29]. MFMT is not a direct imaging technique but relies on solving an inverse problem to form 3-D images of the selected contrast function.

Figure 3. MFMT optical setup accepts the incoming light (EX) after a linear polarizer. The excitation light scanned over the sample with a combination of galvo-mirrors and scanning lens. Backscattered/emission light (EM) is reflected towards detectors with a beam splitter. Prior to the focusing the light with a lens, the backscattered light is filtered and analyzed with an orthogonal polarizer.



Our MFMT system has been described previously in [33] and its schematic is provided in Figure 3. Succinctly, a polarized excitation laser (EX) (658 nm, Thorlabs, USA, L658P040) is fed to a resonant galvo-mirror and focused onto the sample. This was comparable with the bacteria auto-fluorescence band [14] and DiagnodentTM excitation wavelength. Then, backscattered fluorescence emission signal (EM) is captured using the same optical chain in a de-scanned mode. Emission signal is collected by a

linear detector array after a spectral filter and an analyzer (Semrock, USA, FF01-692/LP-25). The detection module consists of 7 Avalanche Photodiode Array (APD) elements (S8550, Hamamatsu, Japan) that is sampled at 1.5 kHz (PCI-6143 DAQ, NI, USA) [31]. Based on the demagnification of the scanning lens, the 7 detectors collect light from 0.8 mm to 3.9 mm away from the irradiated point (*i.e.*, point where light is injected into the sample). In all experiments herein, the field of view (FOV) was set to 4 mm by 6 mm (Figure 1a and 2c), with data collected by the 7 detectors after moving the light injection point every 50 μm along the x-axis, and 30 μm along the y-axis, leading to an array of 80 by 200 positions. A total of 80 by 200 by 7 (112000) measurements were collected at a 7.5 Hz frame rate hardware setting where the resonant mirror operated at 1.5 kHz with a 8.3usec dwell time at each point. Due to the limited sensitivity of APD, 420 frames were averaged to get adequate signal-to-noise ratio (1 min).

2.3. Optical Reconstruction

Once the data was collected, an inverse optical problem was solved to obtain 3-D images of a fluorescent inclusion. As light propagation is still characterized by significant directional anisotropy in the mesoscopic regime, a forward model of light propagation was computed using the Monte Carlo method (MC). There are a few MC-based methods to calculate W . Herein; we employed the forward-adjoint MC method to produce Jacobians [45] for computational efficiency. W is computed by convolving the Green’s functions and the lifetime decay of fluorophore:

$$W(\mathbf{r}_s, \mathbf{r}_d, \mathbf{r}, t) = \int_0^t e^{-\frac{t-t'}{\tau}} dt' \int_0^{t'} G^x(\mathbf{r}_s, \mathbf{r}, t'-t'') G^m(\mathbf{r}, \mathbf{r}_d, t'') dt'' \tag{1}$$

where, G^x and G^m are the time-dependent Green’s functions calculated by MC simulations at the excitation and emission wavelengths, respectively, and τ is the lifetime of the fluorophore. As is customary in FMT and MFMT, the optical properties at the excitation and emission wavelengths are considered to be identical. Moreover, as our data sets are time independent, the formulation of Equation (1) is integrated over time to match our data type. Subsequently, a function that corresponds to changes in fluorescence distribution is calculated using the formulation described in [46]. Briefly, the 3D distribution of the fluorophore’s effective quantum yield $\eta(\mathbf{r})$ can be obtained by solving an integral equation relating the fluorescence signals at time t :

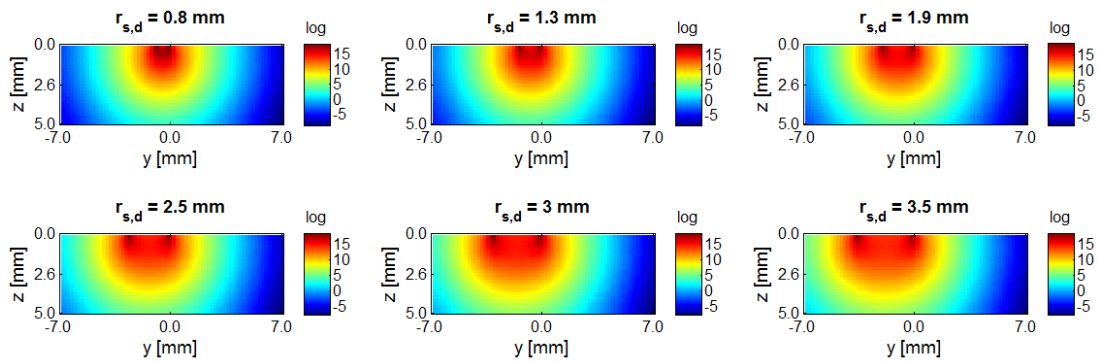
$$U_F(\mathbf{r}_s, \mathbf{r}_d, t) = \int_{\Omega} W(\mathbf{r}_s, \mathbf{r}_d, \mathbf{r}, t) \eta(\mathbf{r}) d\mathbf{r} \tag{2}$$

where $U_F(\mathbf{r}_s, \mathbf{r}_d, t)$ is the fluorescence detected by a detector located at \mathbf{r}_d at t resulting from an excitation at the source, \mathbf{r}_s , at $t=0$, the integration domain, Ω , is defined as the entire imaging volume, and $W(\mathbf{r}_s, \mathbf{r}_d, \mathbf{r}, t)$, referred to as the weight function that describes how a change in $\eta(\mathbf{r})$ will result in a change in $U_F(\mathbf{r}_s, \mathbf{r}_d, t)$.

A system of linear equations describing the relationship between measured signals for each optode combination and the fluorophore distribution can then be solved via a matrix holding the weight function (Jacobian matrix) to obtain $\eta(\mathbf{r})$. *A priori* information required to generate this system are: geometrical information (sample dimensions, location of source/detector pairs, discretization level) and tissue optical properties (μ_s , μ_a and g). Herein, we employed the optical properties of dentin as

reported in the literature [38], *i.e.*, $\mu_s = 28\text{mm}^{-1}$, $\mu_a = 0.3\text{mm}^{-1}$ and $g = 0.93$. To generate a Jacobian with enough statistics, 10^7 photons per source (detector) were simulated. In this study, the volume imaged was discretized in voxels with a size of 200 by 200 by 200 μm^3 . An example of weight functions for the 6 detector positions are provided in Figure 4.

Figure 4. Cross section (yOz , $x = 0$) of Monte Carlo computed sensitivity matrix for different source-detector separation.



In practice, the MFMT image reconstruction process can be expressed using the following equation:

$$\mathbf{x}' = (\mathbf{A}^T \mathbf{A} + \lambda \mathbf{D})^{-1} \mathbf{A}^T \mathbf{b} \quad (3)$$

where \mathbf{x}' is the reconstructed fluorescence distribution $\eta(\mathbf{r})$, \mathbf{A} is the Jacobian obtained from the MC adjoint formulation, \mathbf{b} is a vector containing all measurements. \mathbf{D} is a diagonal matrix whose elements are the square root of the corresponding diagonal element of $\mathbf{A}^T \mathbf{A}$, and λ is a scaling parameter selected via L-curve analysis [47]. The inverse problem was solved using an iterative conjugate gradient method (cgs.m, Matlab). The iterative procedure ended either if 100 iterations or a tolerance of 10^{-2} was reached. Overall, reconstruction procedure took less than 5 min on a personal computer (Intel Core i7 CPU, 2.1GHz, 6G RAM, Windows 7).

We followed a procedure to obtain the best possible data for the reconstruction process. First, the teeth without capillary were imaged to record the background fluorescence signal. Capillaries filled with the selected concentration of dye were then inserted into the hole and the fluorescence signal was acquired by MFMT. And the subtraction process was applied as described in the literature [48]. Lastly, the system dark current was acquired with no light injected into the system. A threshold was applied to all measurements to remove all data whose values were below this dark current noise level.

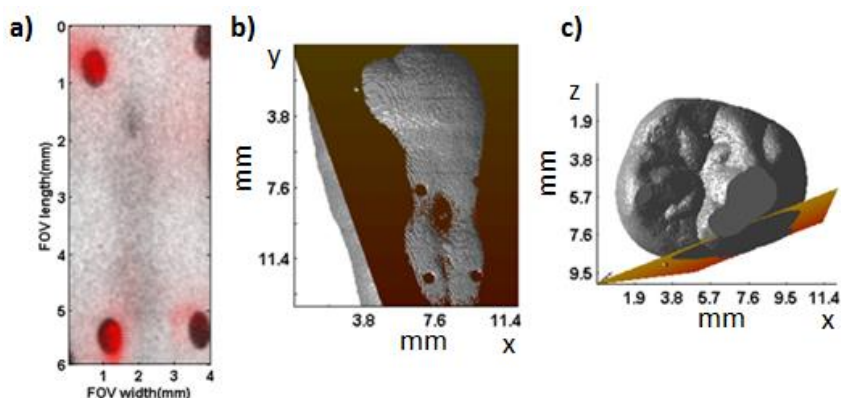
2.4. Image Registration of Multimodal Data Sets

3-D images from both modalities were co-registered in image processing software (Amira 5.6, FEI Visualization Group, France). Teeth were imaged with MFMT and micro-CT, non-concurrently and two data directly overlaid (Figure 5a). The CT image (gray scale image) is shown as the background while the red part represents the MFMT fluorescence background image. Micro-CT image provided the inner-outer structure of teeth as well as the precise 3-D location of the fiducial markers (Figure 5b—capillaries wall). The micro-CT data was down sampled to same discretization level as

MFMT. Doing so enabled a voxel-to-voxel match between the two modalities. Note MFMT and micro-CT initially had voxelization of 200 μm and 38 μm, respectively.

Rigid registration was performed by locating the centers of the 4 fiducial markers of micro-CT and by generating a plane through these locations (Figure 5b,c). This plane corresponds to the outer surface of the sample that was previously used as the boundary condition in the MFMT forward model. Aligning the top layer of MFMT reconstruction with this plane created rotational and transformational registrations of the two data sets. Applying this procedure to all of the five samples ensured that MFMT and micro-CT 3D images were rigidly and accurately co-registered.

Figure 5. (a) Overlaid micro-CT scan and MFMT background image (prior to fluorescence inclusion). (b) Side view of the same plane of tooth, showing alignment marks. (c) Top view of fiducial plane.



3. Results

From all the cases investigated inclusions at 1 mm and 2 mm yielded fluorescence signals that were strong enough to be acquired. All inclusions at 3 mm did not provide adequate signals. To assess the quality of the data sets collected, we compiled the signal-to-noise ratio (SNR) of the measurements after post processing (difference image between fluorescence and background image, Figure 6). In order to mitigate the influence of auto-fluorescence from the markers, the background fluorescence image was processed via histogram equalization first and then segmentation. The region of interest used to calculate the signal and noise intensity was based on the whole binary image. The average signals intensity (root mean square of intensity, RMS) and noise intensity was calculated, respectively. Then, the SNR was estimated as:

$$SNR=10\log_{10} \frac{P_{\text{signal}}}{P_{\text{noise}}}$$

where, the power of signal and noise is estimated through the RMS of the intensities. Table 1 summarizes the SNR of all detectors for the different concentrations/depth combinations.

As expected, the SNR obtained at 1 mm were generally better than the one at 2 mm (average SNR = 18.99 ± 6.24 dB at 1 mm versus 11.17 ± 1.82 dB at 2 mm for 26 μM for instance). Also, the farthest detector yielded the worse SNR overall. However, the 1st detector did not produce the best SNR. For the same concentration, the SNR for the midrange detectors (such as 2nd to 5th detector) are

larger than the other detectors. As described in the previous section, MFMT is a depth resolved imaging technique; this observed SNR behavior is due to the selective depth projection of different source-detector pairs. Higher SNR value in some detectors is an indication of a secondary source, fluorescence concentration, in the corresponding depth. This is expected, as the maximum signal strength is dependent on the best match between the distribution of excitation photons (banana shape) and inclusion location. Hence, detectors close to the source will receive stronger signals from shallow inclusions whereas distant detectors will receive signals from deep inclusions. Note that for certain detectors at 6.5 μM , the signal level was on the same level as noise, leading to $\text{SNR} < 0$.

Figure 6. (a) The raw fluorescence image, wherein the arrow indicates signal. (b) Fluorescence processed data (difference image between the fluorescence signal and fluorescence background).

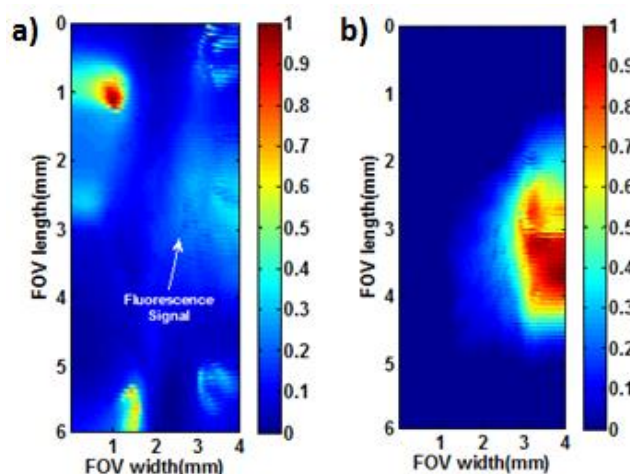


Table 1. SNR of fluorescence signal (dB) for all detectors.

Conc. (μM)	1 mm							2 mm						
	1st	2nd	3rd	4th	5th	6th	7th	1st	2nd	3rd	4th	5th	6th	7th
6.5	<0	<0	<0	<0	<0	<0	<0	0.4	1.2	<0	<0	<0	<0	<0
13	13.5	15.4	12.9	13.7	12.2	11.5	1.9	8.0	9.3	7.8	7.5	7.1	4.3	<0
26	21.5	23.2	23.5	23.5	20.7	12.8	7.7	9.9	11.3	12.8	13.1	11.4	11.9	7.8

Reconstructions from data sets with average SNR above five were performed, also for the special case 2 mm, 6.5 μM . The 3D visualization and co-registration overlay with micro-CT are provided in Figure 7. The MFMT and micro-CT demonstrated a very agreement in all these cases.

In order to evaluate the accuracy of the reconstructed dye distribution, two metrics were computed from the 3-D image data. The first metric is the volume of reconstructed dye distribution. This is compared to dye volume infused into a hollow capillary, which was calculated from its inner diameter and its height. The other parameter is the centroid of dye distribution so as to estimate the spatial accuracy of reconstruction. This parameter was compared with the through-hole center acquired from micro-CT images. Also some adjustments were made due to the edge of bounding box was not exactly the same as the edge of teeth (See Figure 7). Centroid error was calculated as $\max(e_x, e_y, e_z)$. That is to use the maximum value of relative error in each dimension. Table 2 provides the values for this two

metrics for all reconstructions presented in Figure 7. Note that 6.5 μM values are reported at 2 mm whereas not enough signals were collected at 1 mm for the same concentration.

Figure 7. Merged LOT and micro-CT images. (a,b) 1 mm depth hole with concentrations 26 μM and 13 μM respectively. (c,d,e) 2 mm depth hole with concentrations of 26 μM , 13 μM and 6.5 μM .

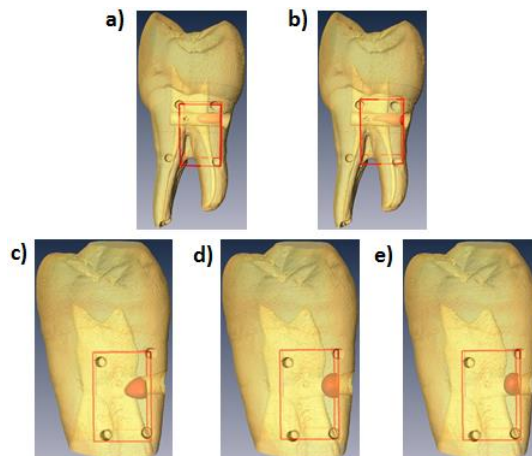


Table 2. Comparison between reconstructed volume and centroid from LOT and micro-CT measurement for the two depths reported.

Dye Concentration (μM)	MFMT Vol. (mm^3)	Micro-CT Vol. (mm^3)	Vol. Error	MFMT Centroid (mm)	Micro-CT Centroid (mm)	Centroid Error	
1 mm	13	2.96	2.67	11%	(2.1, 2.3, -1.0)	(1.7, 2.0, -1.0)	24%
	26	3.18	2.86	11%	(1.6, 2.2, -1.1)	(1.8, 2.0, -1.0)	11%
	6.5	2.34	3.03	23%	(1.9, 2.5, -1.8)	(1.9, 2.4, -2.0)	10%
2 mm	13	2.04	2.67	24%	(1.9, 2.5, -1.8)	(1.7, 2.4, -2.0)	12%
	26	2.90	2.86	1%	(2.1, 2.1, -1.8)	(1.8, 2.4, -2.0)	17%

Overall, MFMT reconstructions were in close agreement with the micro-CT data. Locations in average were retrieved within $\sim 15\%$ error in all cases. Moreover, in the most challenging cases, the MFMT volume was estimated in average with 24% error.

4. Discussion

In this manuscript, we have demonstrated the feasibility of using the laminar optical tomography (LOT) technique in obtaining 3-D fluorescence images in tissues with large absorption and scattering coefficients, such as teeth. This preliminary study demonstrates the possibility of using LOT to enable non-contact and non-invasive imaging for detecting optical changes in teeth at a resolution of 200 μm . This is clinically relevant because some lesions are not observable from tooth surfaces. Contrast created by bacterial activity in sub-surface tooth lesions is simulated using different concentrations of dyes and the site where these metabolic changes occur is simulated by placing the dye at different depths from the tooth surface. The accuracy of reconstruction for LOT was verified by registration with micro-CT images. The errors in placement of dye were estimated by comparing the volume and centroid of reconstructed and real dye distribution in capillary. The average relative error between reconstructed results and real measurements is around 15% for all combinations of depth and dye

concentrations. Meanwhile, the difference between the centroid of reconstructed image and real dye distribution is also less than 0.3 mm in two directions (y and z).

The fluorophore used exhibited high absorption or extinction coefficients ($132,000 \text{ cm}^{-1}\text{M}^{-1}$) from the specification sheet of Alexa Fluoro 660 (LifeTechnologies INC.). Bacterial induced dental lesions (which are a direct or indirect consequence of bacterial colonization) compared with sound teeth can cause a change in absorption and fluorescence that are expected to be at most 10 times larger at peak emission for various wavelength of irradiation [49]. Therefore, the proposed methodology provides a non-radiation technique for identification of the caries lesion of sufficient utility to identify lesions that may not be identifiable utilizing direct visibility. Dental lesions occurring in the fissures of teeth are frequently intact to the visual/tactile examination. The ability to reliably identify tooth loss as deep as 2 mm from the surface and measure volume loss as well as discern bacterial infection can improve the reliability of dental diagnosis. With the ability of the technique to pinpoint the fluorophore to within 0.2 mm of the lesion, is sufficient accuracy to permit the dentist to better localize the location of the carious lesion for a more specific minimal intervention. Lesions at the proximal contact of posterior teeth can only be located utilizing ionizing radiation. A limitation of the ionizing radiation remains that it monitors loss of calcium density, not the penetration of bacteria into the surface. MFMT may permit the identification of cavitated sub-surface lesions that originate within 1.5 mm from the contact, which indicates that many lesions that are not visible on the surface may be detected using the proposed technique. Further studies need to be conducted to determine the depth at which images can be obtained at the contact between teeth.

Additionally, in limited circumstances (*i.e.*, in a single tooth), a lower concentration of dye could be detected at depth of up to 2 mm, but this is not a general case. This is attributed to intra and inter variability of the optical absorption and scattering coefficients of teeth tissues [38]. Such a range of optical properties may lead to two different issues. First, the prior information of tissue optical properties is necessary when using MC method to cast the forward model. Mismatch between the model and sample optical properties could lead to significant errors in the reconstructions. Unfortunately, the optical properties of the dentin and enamel varied largely between different teeth as discussed above (see large deviation [38]). This may be the cause of the errors seen at 2 mm (25% error in volume). Moreover, the external boundaries of the teeth are typically not planar, as modeled in this work. Herein, we have employed a voxel-based MC, but addition of surface profiling and mesh based MC techniques may increase reconstruction accuracy [50]. Second, an increase in attenuation for some specimens leads to less excitation light reaching the fluorophore, resulting in less fluorescence generated. This indicates that more sensitive detectors or higher contrast may be necessary. The current system is based on APD and was designed for fast acquisition of functional signals [31]. The sensitivity of the system can be greatly increased by employing PMTs or other sensitive detectors. Indeed, preliminary tests using an EMCCD (Electron Multiplying CCD) indicate a 2nd order of magnitude increase in sensitivity (results not shown). The system is still being integrated and will be used in subsequent studies. Note also that if Play-Doh was intended as an absorption contrast fiducial, it was found to be fluorescing at the wavelength used. The strong signals from these markers could have led to reduced sensitivity to the weaker signals originating from greater depths. A higher power of light source could also be applied, but in clinical or real application, this would always be limited due to safety considerations. Lastly, the setting of the imaging platform is not appropriate for clinical

application due to the limited space in the human mouth. However, micro-fabricated electromechanical systems (MEMS) based approaches to miniaturize the light source and detector and enhanced sensitivity may enable this application at reduced cost in the future [48]. Combined with fiber, they may allow the implementation of MFMT in articulated arm for easy access to dental tissues [51].

5. Conclusions

Our results demonstrate that MFMT can be used to detect the fluorophore concentration at different depths in excised teeth. This *ex vivo* preliminary indicates that it is possible to get the molecular probe distribution under the surface of teeth up to 2 mm with accuracy, under extremely high and variant optical properties of teeth. Though MFMT detected various concentrations of fluorescent dye placed in teeth, further studies are still needed to insure that the sensitivity of the MFMT can enable detection of naturally occurring lesions in teeth.

Acknowledgments

This work was partly funded by the National Science Foundation NSF CAREER AWARD CBET-1149407, NSF CBET-1263455, and NSF CMMI 1200270. The work was previously presented in SPIE Conference, and it was published in the proceeding as part of SPIE Conference 8937-Multimodal Biomedical Imaging IX [52].

Author Contributions

Feixiao prepared the teeth samples, reconstructed and analyzed images. Mehmet built the LOT system, did the experiment and also performed image reconstruction. Mehmet and Feixiao wrote the first version of the manuscripts under the guidance of Prof. Intes. Prof. Wolff gave advices from the dental profession. Prof. Intes and Prof. Kotha supervised the experiments and revised the paper several times before submission.

Conflict of Interest

The authors declare no conflict of interest.

References

1. Pereira, A.C.; Verdonshot, E.H.; Huysmans, M.C. Caries detection methods: Can they aid decision making for invasive sealant treatment? *Caries Res.* **2001**, *35*, 83–89.
2. Dental Caries (Tooth Decay) in Adults (Age 20 to 64). Available online: <http://www.nidcr.nih.gov/DataStatistics/FindDataByTopic/DentalCaries/DentalCariesAdults20to64.htm> (accessed on 1 May 2014).
3. Haak, R.; Wicht, M.J.; Noack, M.J. Conventional digital and contrast-enhanced bitewing radiograph in the decision to restore proximal carious lesions. *Caries Res.* **2001**, *35*, 193–199.
4. Møystad, A.; Svanaes, D.B.; Risnes, S.; Larheim, T.A.; Gröndahl, H.G. Detection of approximal caries with a storage phosphor system. A comparison of enhanced digital images with dental X-ray film. *Dentomaxillofac Radiol.* **1996**, *25*, 202–206.

5. Tam, L.E.; McComb, D. Diagnosis of occlusal caries: Part II. Recent diagnostic technologies. *J. Can. Dent. Assoc.* **2001**, *67*, 459–463.
6. Park, Y.-S.; Ahn, J.-S.; Kwon, H.-B.; Lee, S.-P. Current status of dental caries diagnosis using cone beam computed tomography. *Imag. Sci. Dent.* **2011**, *41*, 43–51.
7. Hintze, H.; Wenze, A.; Danielsen, B.; Nyvad, B. Reliability of visual examination, Fibre-Optic transillumination, and Bite-wing radiography, and Reproducibility of direct visual examination following tooth separation for the identification of cavitated carious lesions in contacting approximal surfaces. *Caries Res.* **1998**, *32*, 204–209.
8. Wenzel, A. Bitewing and digital bitewing radiography for detection of caries lesions. *J. Dent. Res.* **2004**, *83*, C72–C75.
9. Tyndall, D.A.; Rathore, S. Cone-beam CT diagnostic applications: Caries, periodontal bone assessment, and endodontic applications. *Dent. Clin. North Am.* **2008**, *52*, 825–841.
10. Kamburoğlu, K.; Kurt, H.; Kolsuz, E.; Öztaş, B.; Tatar, I.; Çelik, H.H. Occlusal caries depth measurements obtained by five different imaging modalities. *J. Digit. Imag.* **2011**, *24*, 804–813.
11. Pauwels, R.; Beinsberger, J.; Collaert, B.; Theodorakou, C.; Rogers, J.; Walker, A.; Cockmartin, L.; Bosmans, H.; Jacobs, R.; Bogaerts, R.; *et al.* Effective dose range for dental cone beam computed tomography scanners. *Eur. J. Radiol.* **2012**, *81*, 267–271.
12. David, C.; Christopher, L.; Vincent, P.W.; Bryan, C.; Don, A. Michael pepper three-dimensional terahertz pulse imaging of dental tissue. *J. Biomed. Opt.* **2003**, *8*, 303–307.
13. Smirnov, S.V.; Ya, V.G.; Tsyppkin, A.N.; Bepalov, V.G. Experimental studies of the possibilities of diagnosing caries in the solid tissues of a tooth by means of terahertz radiation. *J. Opt. Technol.* **2014**, *81*, 464–467.
14. Karsten, K.; Herbert, S.; Joerg, H.; Bruce, J.T.; Rudolf, W. Steiner *In-vivo* fluorescence detection and imaging of porphyrin-producing bacteria in the human skin and in the oral cavity for diagnosis of acne vulgaris, caries, and squamous cell carcinoma. *Proc. SPIE* **1994**, *2135*, 129–138.
15. Lussi, A.; Megert, B.; Longbottom, C.; Reich, E.; Francescut, P. Clinical performance of a laser fluorescence device for detection of occlusal caries lesions. *Eur. J. Oral Sci.* **2001**, *109*, 14–19.
16. Shi, X.Q.; Welander, U.; Angmar-Månsson, B. Occlusal caries detection with KaVo DIAGNOdent and radiography: An *in vitro* comparison. *Caries Res.* **2000**, *34*, 151–158.
17. Spitzer, D.; Ten Bosch, J.J. Luminescence quantum yields of sound and carious dental enamel. *Calcif. Tissue Res.* **1997**, *24*, 249–251.
18. Ferreira Zandoná A.; Ando, M.; Eggertsson, H.; Kelly, S.A.; Katz, B.; Eckert, G.; Ofner, S.; Sa, L.; Lukantsova, L.; Wefel, J.S.; *et al.* Clinical Validation of Caries Detection Methodologies: Preliminary Results. *J. Dent. Res.* **2004**, *83*, C84–C88.
19. Sofia, T.; Susan, A.-K.; Stein, B.; Svante, T.; Birgit, A.-M. Application of quantitative light-induced fluorescence to monitor incipient lesions in caries-active children. A comparative study of remineralisation by fluoride varnish and professional cleaning. *Eur. J. Oral Sci.* **2001**, *109*, 71–75.
20. Stookey, G.K. Quantitative light fluorescence: A technology for early monitoring of the caries process. *Dent. Clin. North Am.* **2005**, *49*, 753–770.

21. Chesters, R.K.; Pitts, N.B.; Matuliene, G.; Kvedariene, A.; Huntington, E.; Bendinskaite, R.; Balciuniene, I.; Matheson, J.R.; Nicholson, J.A.; Gendvilyte, A. *et al.* An abbreviated caries clinical trial design validated over 24 months. *J. Dent. Res.* **2002**, *81*, 637–640.
22. Curnow, M.M.T.; Pine, C.M.; Burnside, G.; Nicholson, J.A.; Chesters, R.K.; Huntington, E. A randomised controlled trial of the efficacy of supervised toothbrushing in high-caries-risk children. *Caries Res.* **2002**, *36*, 294–300.
23. Featherstone, J.D.B. The science and practice of caries prevention. *J. Am. Dent. Assoc.* **2000**, *131*, 887–899.
24. Watson, T.F. Fact and artefact in confocal microscopy. *Adv. Dent. Res.* **1997**, *11*, 433–441.
25. McConnell, G.; Girkin, J.M.; Ameer-Beg, S.M.; Baber, P.R.; Vojnovic, B.; Ng, T.; Banerjee, A.; Waston, T.F.; Cook, R.J. Time-correlated single-photon counting fluorescence lifetime confocal imaging of decayed and sound dental structures with a white-light supercontinuum source. *J. Microsc.* **2007**, *225*, 126–136.
26. Lin, P.Y.; Lyu, H.-C.; Hsu Stephen, C.-Y.; Chang, C.-S.; Kao, F.-J. Imaging carious dental tissues with multiphoton fluorescence lifetime imaging microscopy. *Biomed. Opt. Express* **2010**, *2*, 149–158.
27. Holtzman, J.S.; Osann, K.; Pharar, J.; Lee, K.; Ahn, Y.C.; Tucker, T.; Sabet, S.; Chen, Z.P.; Gukasyan, R.; Smith, P.W. Ability of optical coherence tomography to detect caries beneath commonly used dental sealant. *Lasers Surg. Med.* **2010**, *42*, 752–759.
28. Douglas, S.M.; Fried, D.; Darling, C.L. Imaging Natural Occlusal Caries Lesions with Optical Coherence Tomography. *Proc. Soc. Photo Opt. Instrum. Eng.* **2010**, 7549, 75490N.
29. Dunn, A.; Boas, D. Transport-based image reconstruction in turbid media with small source-detector separations. *Opt. Lett.* **2000**, *25*, 1777–1779.
30. Hillman, E.M.C.; Boas, D.A.; Dale, A.M.; Dunn, A.K. Laminar optical tomography: demonstration of millimeter-scale depth-resolved imaging in turbid media. *Opt. Lett.* **2004**, *29*, 1650–1652.
31. Ouakli, N.; Guevara, E.; Dubeau, S.; Beaumont, E.; Lesage, F. Laminar optical tomography of the hemodynamic response in the lumbar spinal cord of rats. *Opt. Express* **2010**, *18*, 10068–10077.
32. Hillman, E.M.C.; Burgess, S.A. Sub-millimeter resolution 3D optical imaging of living tissue using laminar optical tomography. *Laser Photon. Rev.* **2009**, *3*, 159–179.
33. Zhao, L.L.; Lee, V.K.; Yoo, S.S.; Dai, G.H.; Intes, X. The integration of 3-D cell printing and mesoscopic fluorescence molecular tomography of vascular constructs within thick hydrogel scaffolds. *Biomaterials* **2012**, *33*, 5325–5332.
34. Ozturk, M.S.; Lee, V.K.; Zhao, L.L.; Dai, G.H.; Intes, X. Mesoscopic fluorescence molecular tomography of reporter genes in bioprinted thick tissue. *J. Biomed. Opt.* **2013**, *18*, 100501.
35. Yuan, S.; Roney, C.A.; Wierwille, J.; Chen, C.W.; Xu, B.Y.; Griffiths, G.; Jiang, J.; Ma, H.Z.; Cable, A.; Summers, R.M.; Chen, Y. Co-registered optical coherence tomography and fluorescence molecular imaging for simultaneous morphological and molecular imaging. *Phys. Med. Biol.* **2010**, *55*, 191–206.
36. Ozturk, M.S.; Rohrbach, D.; Sunar, U.; Intes, X. Mesoscopic Fluorescence Tomography of a photosensitizer (HPPH) 3D Bio-Distribution in Skin Cancer. *Acad. Radiol.* **2014**, *21*, 271–280.

37. Björn, S.; Englmeier, K.H.; Ntziachristos, V.; Schulz, R. Reconstruction of fluorescence distribution hidden in biological tissue using mesoscopic epifluorescence tomography. *J. Biomed. Opt.* **2011**, *16*, 046005.
38. Fried, D.; Glana, R.E.; Featherstone, J.D.B.; Seka, W. Nature of light scattering in dental enamel and dentin at visible and near-infrared wavelengths. *Appl. Opt.* **1995**, *34*, 1278–1285.
39. Oancea, R.; Podariu, A.C.; Vasile, L.; Rosianu, R.S.; Folescu, R. *In vitro* evaluation of laser fluorescence devices for caries detection through stereomicroscopic imaging. *Rom. J. Morphol. Embryol.* **2013**, *54*, 333–341.
40. Schneiderman, A.; Elbaum, M.; Shultz, T.; Keem, S.; Greenebaum, M.; Driller, J. Assessment of dental caries with digital imaging fiber-optic Transillumination (DIFOTITM): *In vitro* study. *Caries Res.* **1997**, *31*, 103–110.
41. Lee, C.; Darling, C.L.; Fried, D. *In vitro* near-infrared imaging of occlusal dental caries using germanium enhanced CMOS camera. *Proc. Soc. Photo. Opt. Instrum. Eng.* **2010**, *7549*, 1–7.
42. Ko, A.C.-T.; Choo-Smith, L.P.; Hewko, M.; Leonardi, L.; Sowa, M.G.; Dong, C.C.S.; Williams, P.; Cleghorn, B. *Ex vivo* detection and characterization of early dental caries by optical coherence tomography and Raman spectroscopy. *J. Biomed. Opt.* **2005**, *10*, 031118.
43. Choo-Smith, L.P.; Hewko, M.D.; Dufour, M.L.; Fulton, C.; Qiu, P.L.; Gauthier, B.; Padioleau, C.; Bisailon, C.E.; Dong, C.; Cleghorn, B.M.; *et al.* *Ex vivo* imaging of early dental caries within the interproximal space. *Proc. SPIE* **2009**, doi:10.1117/12.809553.
44. Shi, X.Q.; Welander, U.; Angmar-Mansson, B. Occlusal caries detection with KaVo DIAGNOdent and radiography: An *in vitro* comparison. *Caries Res.* **2000**, *34*, 151–158.
45. Chen, J.; Intes, X. Comparison of Monte Carlo methods for fluorescence molecular tomography-computational efficiency. *Med. Phy.* **2011**, *38*, 5788–5798.
46. Chen, J.; Venugopal, V.; Intes, X. Monte Carlo based method for fluorescence tomographic imaging with lifetime multiplexing using time gates. *Biomed. Opt. Express* **2011**, *2*, 871–886.
47. Intes, X.; Ripoll, J.; Chen, Y.; Nioka, S.; Yodh, A.G.; Chance, B. *In vivo* continuous-wave optical breast imaging enhanced with Indocyanine Green. *Med. Phys.* **2003**, *30*, 1039.
48. Muldoon, T.J.; Burgess, S.A.; Chen, B.R.; Ratner, D.R.; Hillman, E.M.C. Analysis of skin lesions using laminar optical tomography. *Biomed. Opt. Express* **2012**, *3*, 1701–1712.
49. Cui, W.; Kurnar, C.; Chance, B. Experimental study of migration depth for the photons measured at sample surface. *Proc. SPIE* **1991**, *1431*, 180–191.
50. Chen, J.; Fang, Q.; Intes, X. Mesh-based Monte Carlo method in time-domain widefield fluorescence molecular tomography. *J. Biomed. Opt.* **2012**, *17*, 106009.
51. Burgess, S.A.; Ratner, D.; Chen, B.R.; Hillman, E.M.C. Fiber-optic and articulating arm implementations of laminar optical tomography for clinical applications. *Biomed. Opt. Express* **2010**, *1*, 780–790.
52. Long, F.; Mehmet, S.O.; Xavier, I.; Shiva, K. Dental imaging using laminar optical tomography and micro CT. *Proc. SPIE* **2014**, doi:10.1117/12.2037766.